FLUID STRUCTURE INTERACTION INVESTIGATION OF THE AERODYNAMIC CHARACTERISTICS OF A DYNAMIC CAMBER MORPHING AND PITCHING ROTOR AIRFOIL

Muhammed Kürşat Yurt * Amine Abdelmoula † Jonas John ‡ İlkay Yavrucuk §
Institute for Helicopter Technology and VTOL
Technical University of Munich, 80333 Munich, Germany

This paper presents an extensible fluid-structure interaction (FSI) framework to investigate unsteady aerodynamic characteristics of pitching and dynamically camber morphing airfoils. An in-house finite element method-based Euler beam model was developed in this study to model the structure. The aerodynamic loads were computed with the computational fluid dynamics solver SU2. The coupling framework exploits the multiphysics coupling library preCICE for data exchange, converge accelerations, and implicit coupling logic. Both developed structural solver and coupling framework were validated with available data from the literature. The FishBAC deformation was applied from 75% to 90% of the chord length. An investigation of steady-state FSI coupling was conducted from Mach number 0.1 to 0.4 to show how the aeroelastic effects evolve for an actively morphing airfoil.The results showed that the camber morphing section of the presented structural model deformed in an aeroelastic manner under the influence of aerodynamic loads, and the morphed shape changed significantly. Moreover, unsteady aerodynamics and FSI effects on both pitching and actively morphing airfoils were investigated at Mach 0.4 and a pitching frequency of 7 Hz. This study showed the importance of considering aeroelastic effects on the unsteady aerodynamic characteristic. It was shown that the active camber morphing section could not be considered rigid. The aeroelastic effects became more pronounced with increasing Mach number and must be modeled.

1 INTRODUCTION

Rotorcraft operate in diverse flight conditions, necessitating the main rotor to contend with varying aerodynamic environments. These conditions, such as hover or high-speed forward flight, impose different demands on rotor performance. For instance, in forward flight, the flow characteristics at each blade section, determined by rotor azimuth and radial position, span a wide range of angles of attack and velocities, including reverse flow. Rotor blades in fast-forward flight experience varying blade tip Mach numbers, with higher values on the advancing side. To optimize performance, the advancing rotor blade benefits from a high drag divergence Mach number on the outboard sections and high maximum lift coefficients on the retreating side, complemented by moderate twist. Conversely, hover conditions feature lower blade tip Mach numbers, necessitating higher blade twists for improved performance. Achieving an optimal rotor design entails a trade-off, balancing overall performance with aerodynamic efficiency for a specific flight state. Modern rotor designs address these diverse requirements by incorporating different airfoil sections along the blade

* Graduate Research Assistant
† Graduate Research Assistant
‡ Graduate Research Assistant
§ Professor and Department Head

radius. The ability to dynamically adapt the shape of sections in response to flight conditions, thereby adjusting rotor aerodynamic characteristics, holds promising potential for enhanced efficiency, reduced greenhouse gas emissions, greater lift capability, and increased maximum flight speed. In comparison to conventional trailing edge flaps, the morphing of a parabolic camber variation has shown improvements in lift-to-drag ratios while maintaining a constant lift. Flight tests conducted by Roth [1] in 2006 successfully demonstrated the effectiveness of active parabolic trailing edge flaps in suppressing hub vibrations occurring at a rate of 4 per revolution by means of piezoelectric actuated trailing edge flaps. Hunsaker et al. [2] explored the concept of camber morphing for fixed-wing airfoils and demonstrated that applying a continuous parabolic deflection on the airfoil profile can lead to a significant decrease in drag compared to a plain flap. Woods et al. [3] introduced the Fish Bone Active Camber (FishBAC) design concept, depicted in Figure 1, which has been the subject of recent studies [3–8]. Rauleder et al. [9] and Komp et al. [10–12] investigated the dynamic morphing of the BO105 blade section using the FishBAC concept across various advanced ratios μ ranging from 0 to 0.35. These studies utilized CAMRAD II as a comprehensive analysis tool and demonstrated that the dynamic morphing of the camber results in a redistribution of thrust over the rotor disk, leading to a power reduction of up to 7.5% compared to the baseline rotor blade of the BO105 at an advance ratio of 0.35. Kumar et al. [13] utilized the same setup and showed that for medium advance ratios ($\mu = 0.10$ and $\mu = 0.15$), dynamically morphing the airfoil of the baseline blade can reduce aeroacoustic noise, rotor hub vibration, and the required rotor power. In these studies, steady airfoil tables were utilized to calculate rotor aerodynamics. However, Abdelmoula et al. [14] demonstrated that steady-state airfoil data alone is insufficient for accurately modeling airfoil properties in helicopter applications involving high-frequency pitching and morphing oscillations. They found that significant deviations in aerodynamic loading behavior occurred due to unsteadiness, as observed through Computational Fluid Dynamics (CFD) investigations.

Additionally, previous research has primarily focused on investigating the fluid-structure interaction of FishBAC with mid-fidelity steady aerodynamic models limited to a low Mach number range ($M < 0.2$). These studies have revealed that the amount of moment needed to morph a non-pitching baseline airfoil using the FishBAC concept increases as the aerodynamic forces act along the airfoil surface. The extent of static morphing plays a role in determining this increase. Consequently, the camber morphing section cannot be considered completely rigid when subjected to aerodynamic loads, as the elastomeric skin, tendons, spine, and stringer - illustrated in Figure 1 - possess elastic properties.

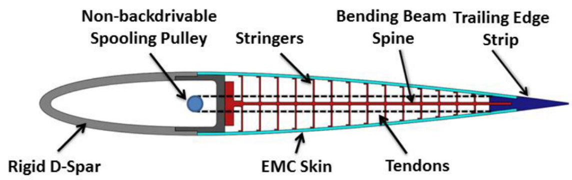

Fig. 1: Fish Bone Active Camber (FishBAC) design concept [6].

The objective of this study is to demonstrate the variations in camber morphing shape for the FishBAC concept as the free stream velocity under the incompressible and the compressible flow regime. To achieve this goal, a tightly coupled, high-fidelity fluid-structure interaction framework is introduced to showcase how structural deformation impacts the aerodynamic behavior of the airfoil. Initially, an investigation was conducted to examine how steady loads lead to changes in the camber shape and the trailing deflection, attributed to the response of the elastic structure to these steady loads. Subsequently, the study explores the morphing of the camber section while the FishBAC airfoil undergoes simultaneous morphing and pitching. The primary objective of this investigation is to demonstrate how fluid-structure interaction influences airfoil characteristics, particularly when considering unsteady aerodynamic loads resulting from both pitch and active camber morphing.

2 METHODOLOGY

In this section, the structural modeling methodology employed in this paper is explained. Subsequently, the CFD methodology and the meshing strategy that is adopted will be explained. The subsequent section will provide insights into the design and workflow of the coupling framework. Finally, the last section provides the details of active morphing schedule that is applied in this study.

2.1 STRUCTURAL MODELLING

The FishBAC active camber concept consist of three main components, namely, a rigid leading part, a morphing middle section and a rigid trailing edge, as seen in Figure 1. The middle section is composed of several structural elements that enable active morphing capability. The primary component of the morphing section consists of a flexing spine that imparts rigidity and provides support to the airfoil. The spine runs along the length of the middle section and maintains the overall structural integrity during the morphing process. The stringers, are the structural elements perpendicular to the spine and provide the support for the elastic skin. The skin covers and encloses the structural elements and provides a smooth surface, which is essential for aerodynamic profile.

The structural behaviour of the morphing section of the airfoil has been modelled using the Finite Element Method (FEM). The structure is modelled with Euler-Bernoulli beam elements. This approach is suggested and applied by Woods et al. [8], and proved to successfully model the structural behaviour of the mechanism. The sectional flexural rigidity is obtained as a summation of the flexural rigidities of the individual structural elements of the given section, calculated as follows:

$$EI_{\text{total}} = EI_{\text{spine}} + EI_{\text{skin}} + EI_{\text{stringer}} \tag{1}$$

where the structural rigidity of the spine is given in terms of elastic modulus of material used in the bending-spine (E_{spine}), the span of the wing segment b, and thickness of the bending-spine t_{spine}.

$$EI_{\text{spine}} = \frac{E_{\text{spine}}}{12} t_{\text{spine}}^2 b \tag{2}$$

The elastic skin, although possessing lower rigidity, contributes to the flexural rigidity due to its attachment at a considerable distance away from the neutral axis of the bending spine. Using the parallel-axis theorem one can formulate the contribution as follows, in terms of elastic modulus of material used in the skin (E_{skin}), the span of the wing segment b, and thickness of the skin t_{skin}, and distance of upper and lower skin from the neutral axis r_{up}, and r_{low}.

$$EI_{\text{skin}} = E_{\text{skin}} t_{\text{skin}}^3 b \left[\frac{1}{6} + r_{\text{up}}^2 + r_{\text{low}}^2 \right] \tag{3}$$

In this formulation, it is assumed that the thickness of the skin is the same for both upper and lower surfaces. The contribution of the stringers is also included in a similar manner as described above:

$$EI_{\text{stringer}} = \frac{E_{\text{stringer}}}{12} t_{\text{stringer}}^3 b \tag{4}$$

Additionally, to account for the time-dependent structural dynamic behavior, mass properties for each section of the active camber concept are required. The sectional mass per unit length, denoted as $\bar{m}_{\text{total}}$, is the sum of the sectional mass contributions arising from three key structural elements: the bending spine, the skin, and the stringer. The mass properties are determined by the following equations:

$$\bar{m}_{\text{total}} = \bar{m}_{\text{spine}} + \bar{m}_{\text{skin}} + \bar{m}_{\text{stringer}} \tag{5}$$

The sectional mass contribution of the bending spine, denoted as $\bar{m}_{\text{spine}}$, is expressed in terms of the material density ρ_{spine}, the span of the wing segment b, and the thickness of the bending-spine t_{spine}:

$$\bar{m}_{\text{spine}} = \rho_{\text{spine}} t_{\text{spine}} b \tag{6}$$

Similarly, the contribution of both the upper and lower skin sections is given by:

$$\bar{m}_{\text{skin}} = 2\rho_{\text{skin}} t_{\text{skin}} b \tag{7}$$

Finally, the sectional mass contribution of the stringer represented as $\bar{m}_{\text{stringer}}$, is defined as:

$$\bar{m}_{\text{stringer}} = \rho_{\text{stringer}} t_{\text{stringer}} b \tag{8}$$

The mass properties are essential for accurate modeling of the active camber concept's time-dependent structural dynamics and the comprehensive analysis of its intricate morphing behavior.

After the properties of the beam model are defined, an in-house finite element solver is utilized for solving. The implemented elemental mass and stiffness matrices K_e, M_e are given as follows:

$$K_e = \frac{EI}{L^3} \begin{bmatrix} 12 & 6L & -12 & 6L \\ 6L & 4L^2 & -6L & 2L^2 \\ -12 & -6L & 12 & -6L \\ 6L & 2L^2 & -6L & 4L^2 \end{bmatrix} \tag{9a}$$

$$M_e = \frac{\bar{m}L}{420} \begin{bmatrix} 156 & 22L & 54 & -13L \\ 22L & 4L^2 & 13L & -3L^2 \\ 54 & 13L & 156 & -22L \\ -13L & -3L^2 & -22L & 4L^2 \end{bmatrix} \tag{9b}$$

The solver uses a second order Newmark-β [15] time integration scheme for time-stepping with parameters $\beta = 0.25$, and $\gamma = 0.5$. Note that there is no structural damping modeled in the current study.

2.2 AERODYNAMIC MODELLING

The aerodynamic loads on the structure are evaluated using the SU2 code [16]. An O-type structured grid topology is employed for meshing to ensure an accurate representation of the flow characteristics. The airfoil surfaces are meticulously discretized, resulting in a total of 500 grid points strategically distributed to effectively capture the airfoil's geometry and flow behavior near the surface. To account for three-dimensional flow phenomena, the surface mesh is extruded in the normal direction to the airfoil surface, extending up to a distance of 150 chord lengths. The meshes employed in the simulations comprised 71,116 quadrilateral structured cells exhibiting high orthogonality. A detailed view of the mesh near the airfoil surface for NACA23012 simulations is shown in Figure 2. A crucial criterion of $y^+ < 1$ is met throughout the simulations, indicating that the non-dimensional wall distance is appropriately chosen to effectively resolve the boundary layer near the airfoil surface.

Regarding the turbulence modeling, the airfoil surface is treated as a fully turbulent viscous wall, and the one-equation Spalart–Allmaras turbulence model is implemented to solve the transport equation for the eddy viscosity.

A grid deformation approach is utilized to capture the pitching motion and structural deformation of the airfoil, ensuring a comprehensive representation of the fluid-structure interaction.

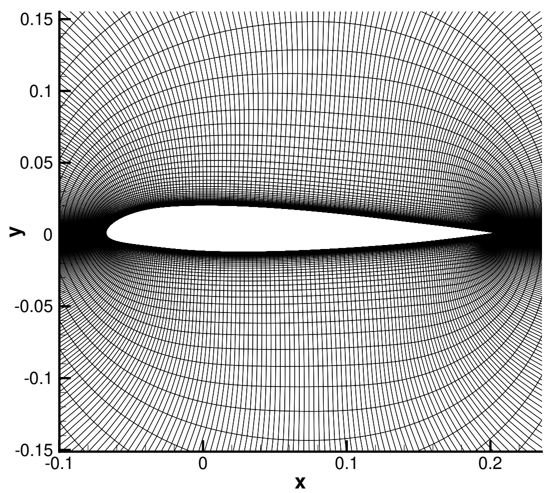

Fig. 2: CFD grid near the airfoil.

2.3 AEROELASTIC COUPLING

In the aeroelastic coupling framework, for data exchange, convergence acceleration, and implicit coupling logic, the open-source multiphysics library preCICE [17] is used.

The coupling flow starts with the initialization of both solvers. After initialization for the start time, the structural problem is solved with the actuation moment. The obtained deflection and rotation of the spine from the structural problem are mapped to the surface as displacements. The displacement data is transferred by preCICE to the fluid solver. The fluid solver deforms the mesh for the given input displacements using an elasticity analogy explained in [16, 18].

After the aerodynamic solutions are obtained, preCICE checks for convergence of aerodynamic forces and displacement fields. The L2 norm of the absolute difference between the two iterations is set to 0.5 and 0.001, respectively, for force and displacement fields. If the convergence is achieved, the simulation advances to the next time step or exits for steady-state couplings, as depicted in Figure 3.

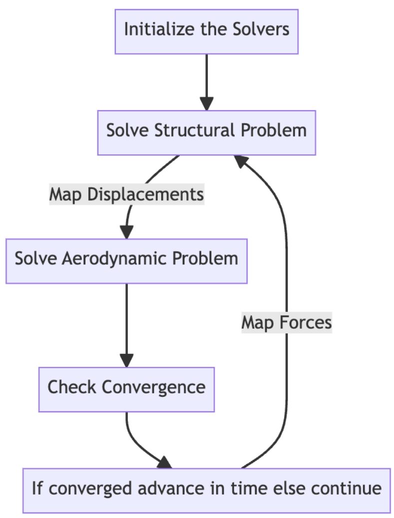

Fig. 3: Flowchart of the coupling framework.

2.4 ACTUATION PROFILE

The target deflection schedule is depicted in Figure 4. This profile has been extracted from the study conducted by Komp et al. [19], where it has been found to yield optimum rotor power saving through camber morphing actuation at a specific advance ratio of $\mu = 0.15$. The actuation profile is mathematically defined by Eq. (10), and the corresponding actuation inputs can be found in Table 1. This profile serves as a fundamental basis for our investigation, allowing us to analyze the efficacy of camber morphing in achieving desired aerodynamic performance improvements.

$$\delta = \delta_{0P} + \sum_{n=1}^{2} \delta_{nP} \cdot \cos(n\psi - \phi_{nP}) \tag{10}$$

Table 1: Actuation inputs used in this study.

δ_{0P}	ϕ_{1P}	δ_{1P}	ϕ_{2P}	δ_{2P}
2.65°	299°	2.22°	249°	0.65°

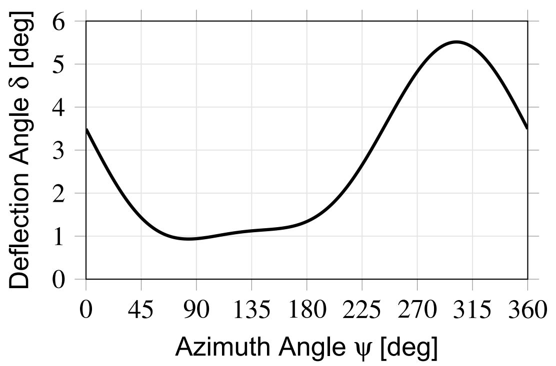

Fig. 4: Target deflection schedule.

The target deflection schedule was presented in Figure 4. In the case of static simulations, it is observed a linear correlation between the applied actuation moment and the resulting deflection angle, see Figure 5. For standalone CFD simulations, the applied moment was calculated using this linear relationship and the target deflection angle. In the standalone CFD approach, the computed shapes are directly generated by the structural solver after applying the bending moment. In the steady FSI scenario, the aerodynamic loads obtained from these shapes are fed back to the structural solver to determine the new shapes for the next steady CFD run.

Similarly, for the unsteady investigations, the deflection angle schedule is mapped to an applied moment schedule. In standalone CFD simulations, the morphed airfoil shape is obtained from the steady state structural simulation, and passed to the CFD solver at every time step. In the unsteady FSI, the structural deformation of the morphing section is computed using an unsteady model. Within every time step, aerodynamic forces and structural deformation iteratively exchanged until the forces and the deformation reach convergence.

This approach allowed for a comprehensive investigation of the fluid-structure interaction with the dynamic actuation of the airfoil, thereby providing valuable insights into the morphing process.

3 RESULTS AND DISCUSSION

In this section, both the developed in-house structural solver and the coupling framework are validated against experimental and computational data available in the literature. The steady-state FSI and CFD standalone analyses are conducted for a NACA23012 airfoil at Mach numbers ranging from 0.1 to 0.4. In the last section, unsteady aerodynamic characteristics of pitching and actively morphing and pitching airfoils were investigated at Mach number 0.4.

3.1 VALIDATION OF STRUCTURAL MODEL

The in-house structural solver is subjected to a validation process against experimental data conducted by Woods et al. [8]. The validation included two distinct configurations, one with the elastic skin attached to the FishBAC structure and the other without the skin attachment. The structural properties of the FishBAC, as detailed in Table 2, are used in the simulations.

The validation results, depicted in Figure 5, revealed a good level of agreement between the numerical predictions obtained from the developed structural solver and the corresponding experimental measurements. In particular, good conformity is observed in most cases.

It is important to mention that the most notable deviation between the numerical and experimental results was noticed in the scenario without the skin attachment and under the influence of an applied tip force. However, it is worth noting that without a skin attached, the model does not reflect the operational condition as skin is not attached. Also, it is relevant for the validation of the presented work since the primary focus of the investigation is the behavior of the model under fluid-structure interaction in operational conditions.

3.2 VALIDATION OF FSI FRAMEWORK

Additional validation is performed to ensure an accurate exchange of data between the fluid and the structure solvers with the developed framework. For this purpose, the data presented by Woods et al. [8]

Table 2: Structural Properties of Validation Case.

Parameter	Value
Airfoil	NACA0012
Chord c	305 mm
Span b	150 mm
Start of morphing section	0.35c
End of morphing section	0.85c
Spine thickness	2 mm
Stringer thickness	0.8 mm
Skin thickness	1.5 mm
Spine modulus	2.14 GPa
Stringer modulus	2.14 GPa
Skin modulus	4.56 MPa
Number of stinger pairs	14

was taken as reference. The operational conditions are provided in Table 3.

As demonstrated in Figure 6, the lift coefficient predictions exhibit a good level of agreement, with the differences between the two frameworks remaining within acceptable bounds even when an applied moment is introduced. The observed difference does not exceed 7%, affirming the robustness of our approach in simulating the fluid-structure interaction phenomenon.

The most significant difference arises in the prediction of the steady drag coefficient. This discrepancy can be attributed to the distinct boundary layer modeling approaches employed in the two frameworks.

While the results are computed in [8] used XFoil [20] to model the boundary by means of a e^n transition method, the current CFD setup adopts a fully turbulent wall modeling approach. This creates an offset in low-speed aerodynamic flows, as evident in this validation case.

Overall, despite the observed differences in the drag coefficient prediction, the validation results reinforce the credibility and accuracy of the currently developed framework in simulating fluid-structure interactions of elastic airfoil structures. The satisfactory agreement in lift coefficient predictions further confirms the validity of our approach and supports its application in rotorcraft design and analysis.

Table 3: Operation point of the Validation Case.

Parameter	Value
Freestream velocity	20 m/s
Reynolds number	240,000
Angle of attack	5°

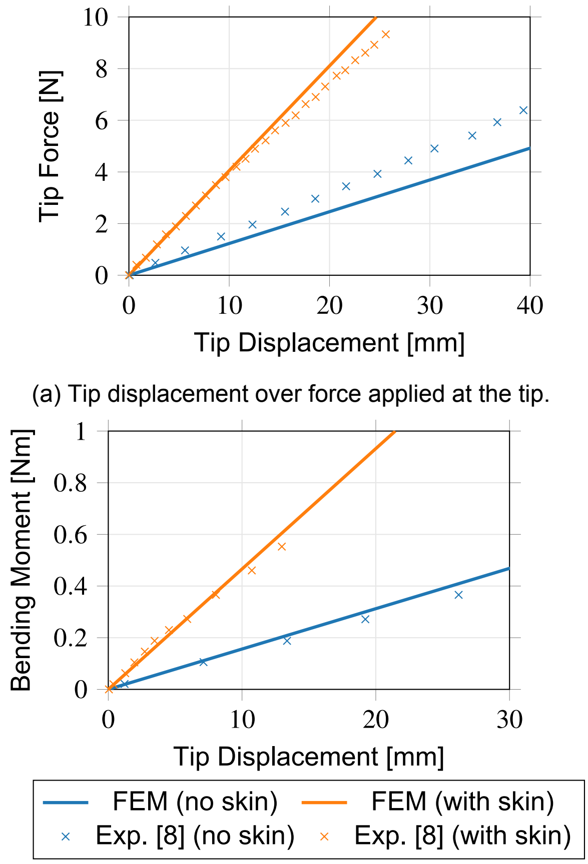

(a) Tip displacement over force applied at the tip.

(b) Tip displacement over moment applied at the tip..

Fig. 5: Validation of the structural modelling strategy against experimental data from the literature.

3.3 STEADY STATE FSI OF NACA23012 AIRFOIL

In this section, the steady-state deformation of a NACA23012 airfoil is investigated. The structural modeling approach and Fluid-Structure Interaction (FSI) framework used in the study are validated in the Sections 3.1 and 3.2. In this study, the free-stream Mach number is varied from 0.1 to 0.4 to investigate its effect on the aerodynamic coefficients and shape of the camber morphing section. The different flow conditions considered are listed in Table 5.

The study depicted in Figure 7a focuses on analyzing the lift coefficient's variation with respect to the bending moment for two distinct cases. The first case is simulated with the shapes obtained from structural deformation without including aerodynamic loading on the structure, illustrated by dashed lines and denoted by "CFD". The other case is simulated with considering the aerodynamic forces applied on the structure to obtain a steady-state equilibrium position, illustrated by continuous lines and denoted by "FSI". For the CFD cases, the slope of the lift coefficient curve increased by 15% with increasing

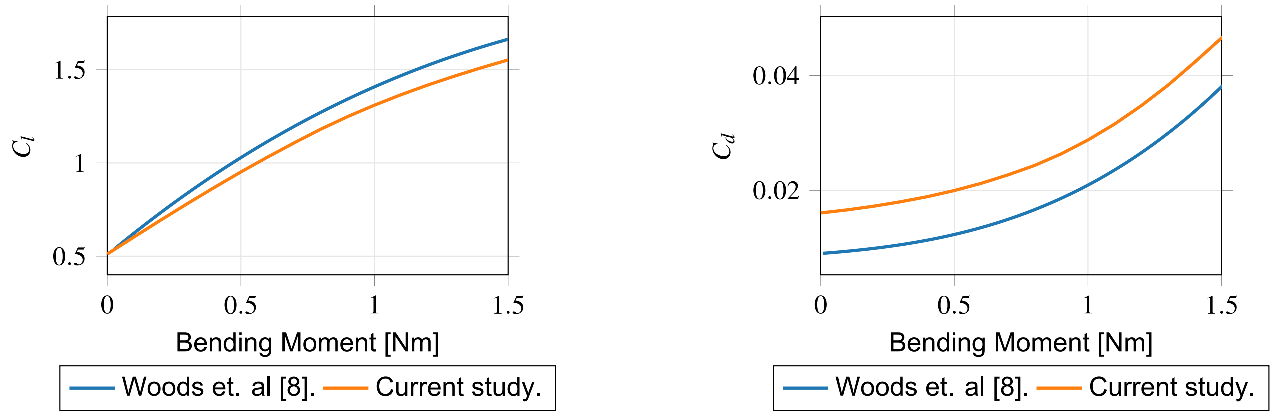

(a) Steady lift coefficient over applied actuation moment.

(b) Steady drag coefficient over applied actuation moment.

Fig. 6: Validation of the FSI framework aerodynamics coefficients.

Table 4: Structural Properties of the current case.

Parameter	Value
Airfoil	NACA23012
Chord c	270 mm
Span b	1 m
Start of morphing section	0.75c
End of morphing section	0.90c
Spine thickness	0.75 mm
Stringer thickness	1 mm
Skin thickness	0.5 mm
Spine modulus	28 GPa
Stringer modulus	2.1 GPa
Skin modulus	1.22 MPa
Spine density	1580 kg/m^3
Stringer density	1070 kg/m^3
Skin density	315 kg/m^3
Number of stinger pairs	4

Table 5: Flow conditions for the steady-state simulations.

Parameter	Value
Mach Number	[0.1,0.2,0.4]
Freestream Temperature	15° C
Freestream Angle of Attack	4°

flow velocity from $M = 0.1$ to $M = 0.4$. However, for the FSI cases, this trend reversed. The slope of the lift coefficient curve decreased by 45% with rising velocity.

At a low Mach number of $M = 0.1$, there were only slight differences observed between the coupled and uncoupled simulations in terms of lift approximation, even as the bending moment increased. As the Mach number increased, the disparity between the modeling approaches became more significant with the increasing bending moment. This difference was most pronounced at a Mach number of $M = 0.4$, where the variation in C_l amounted to $\Delta C_l = 0.28$ for a bending moment of 6 Nm.

As shown in Figure 7b, the drag coefficient followed similar trends. At the low Mach number $M = 0.1$, the maximum difference is $\Delta C_d = 0.001$, which is in good agreement with the uncoupled simulations. However, at higher Mach number $M = 0.4$, the deviation increased to $\Delta C_d = 0.003$.

Figure 7c shows the equlibrium shapes of the airfoil when an actuation moment of 6Nm was applied at different Mach numbers. The results shown that the morphing section of the airfoil, under the influence of the aerodynamic loads, could not provide targeted shapes. It was found that the deviation between the deflection angle of the target shape and the equilibrium shape could be up to 5 degrees.Therefore, the aeroelastic effects must be taken into consideration when applying the active camber morphing concept.

3.4 UNSTEADY FSI OF NACA23012 AIRFOIL

In this section, the combined effect of morphing and pitching on the unsteady aerodynamic characteristics of the baseline airfoil, NACA23012, will be investigated. The pitching motion of the airfoil is described by the following equation:

$$\theta = \theta_{\text{mean}} + A \cdot \sin(2\pi f t) \tag{11}$$

where θ_{mean} represents the mean pitching amplitude, f is the pitching frequency in herz, t is the time, and A is the pitching amplitude. A time discretization corresponding to 720 time steps per revolution is selected. Ten pitching periods were simulated

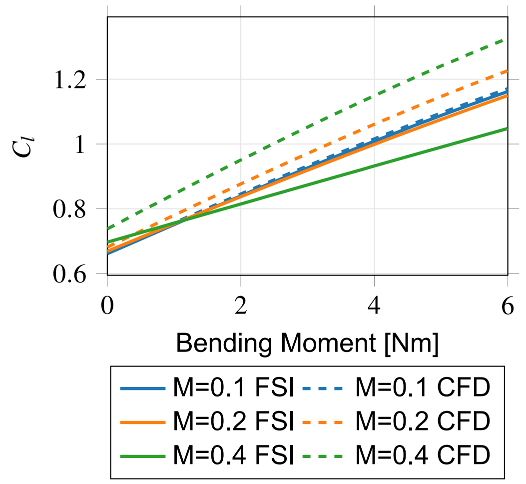

(a) Change of aerodynamic lift coefficient with respect to applied bending moment for different free-stream Mach numbers.

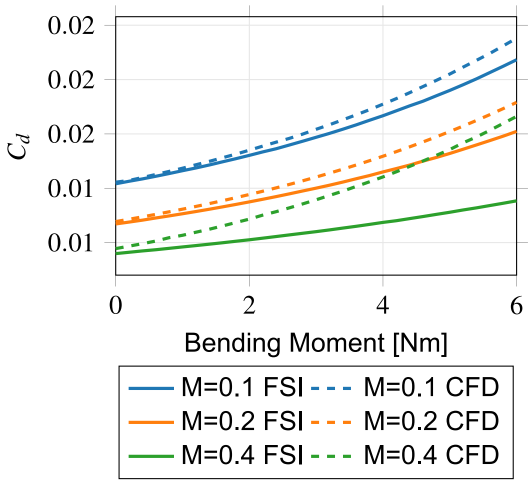

(b) Change of aerodynamic drag coefficient with respect to applied bending moment for different free-stream Mach numbers.

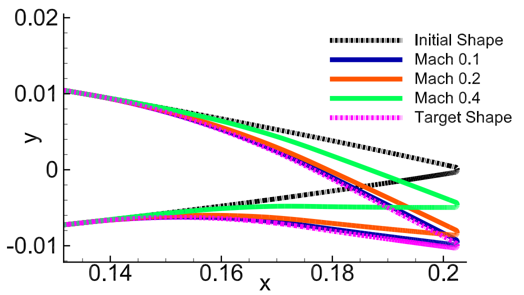

(c) Equilibrium shapes for actuation moment of 6 Nm for different free-stream Mach numbers.

Fig. 7: Change of aerodynamic coefficients and morphed equlibrium shapes at different Mach numbers.

for each study. For uncoupled CFD simulation convergence in aerodynamic coefficients C_l, C_d, and C_m was obtained after four pitching cycles. For the unsteady coupled, the convergence was reached after a seven pitching cycles. The operating point is given in Table 6.

Table 6: Unsteady operating point.

Parameter	Value
Mach Number	0.4
Freestream Temperature	15° C
θ_{mean}	4°
Pitching amplitude	4°
Pitching frequency	7 Hz

In this section, two cases are investigated: First, the pitching of the airfoil was simulated without dynamic morphing, and then the airfoil was actively morphed and pitched simultaneously. For these two different scenarios, the effect of aeroelasticity was analyzed by the comparison of the aerodynamic coefficients obtained with and without FSI coupling based on the approach explained in Section 2.

Figure 8 shows the change in the unsteady lift coefficient. It was shown that for both cases, pitching and pitching with active morphing, the most significant FSI effect is observed at the highest pitch angle. For the active case, this difference is significantly greater with $\Delta C_l = 0.18$ than for the pitching case with $\Delta C_l = 0.05$. For both cases, at the minimum pitching angle, the difference is lower with 0.06 and 0.02 for the active and pitching cases, respectively. In these two cases, the slope of the lift coefficient curve decreases. In addition to the change of the slope, the shape of the hysteresis has also changed in the active case due to the complex interaction between the fluid and the structure.

The pitching moment coefficient also shows a significant change in aerodynamic characteristics, as shown in Figure 9. For the pitching case, it was found that the FSI simulation yields higher pitching moment values than the CFD single simulation. Moreover, the pitching moment slope increases when FSI effects are included, resulting in undesirable positive values of the pitching moment coefficient. However, these trends are observed in pitching with blades reverse when pitching is combined with active morphing, as shown in Figure 9b. In both cases, the pitching moment coefficients are negative over the entire pitching angle range. However, the magnitude of the pitching moment was larger than in the cases where only pitching motion was considered, which

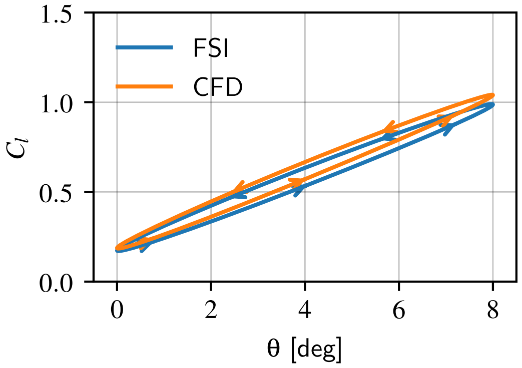

(a) Pitching Airfoil

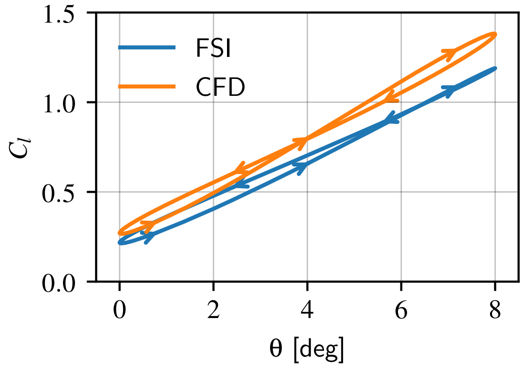

(b) Pitching with Actively Morphing Airfoil

Fig. 8: Unsteady variation of aerodynamic lift coefficient during unsteady motion of the airfoil at M=0.4.

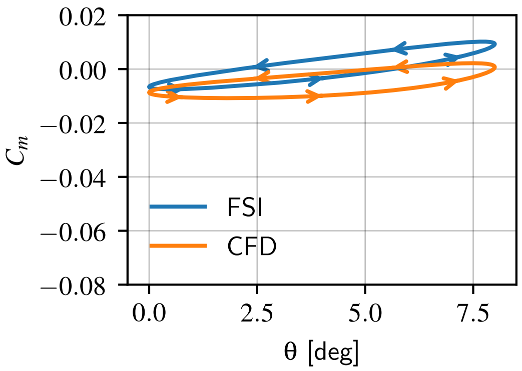

(a) Pitching Airfoil

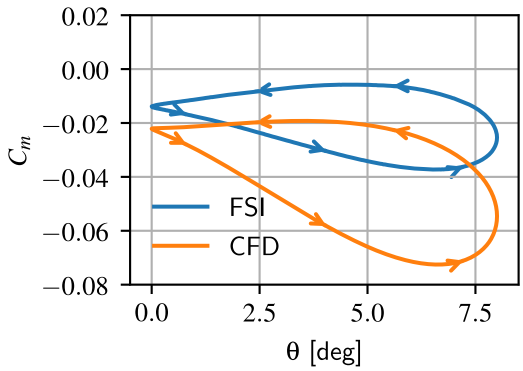

(b) Pitching with Actively Morphing Airfoil

Fig. 9: Unsteady variation of aerodynamic pitching moment coefficient during unsteady motion of the airfoil at M=0.4.

may cause higher root stresses at the blade root and the control joints [21]. Note that, in the FSI case, there was a shift toward a smaller negative pitching moment coefficient than in the CFD case. In addition, the hysteresis phenomenon was strongly enhanced when the airfoil was actively morphing. The result shows that when modeling the aerodynamics of actively morphed blades for rotor applications, not only the unsteady effects, as shown by Abdelmoula et al. [14], but also the fluid-structure interaction must be considered.

4 CONCLUSIONS

In this work, the development of a partitioned FSI analysis framework for pitching and morphing airfoils was presented. The CFD solver SU2 was used to solve the fluid dynamic problem and to calculate the aerodynamic load acting on the airfoil surface. At the same time, an in-house FEM-based Euler beam model was developed and used to solve the structural dynamic problem. The obtained results showed that the developed structural solver has a good level of accuracy compared to the experimental data. In addition, the proposed coupling framework exhibits a very good degree of accuracy compared to the previous work.

The investigations indicate that with the increasing flow velocity, aerodynamic forces play an important role in the structure and change the response. In particular, as Mach number increases, these effects become more significant. As the flow velocity transitioned from $M = 0.1$ to $M = 0.4$, the slope of the lift coefficient curve increased by 15%. In contrast, including fluid-structure interaction resulted in a 45% decrease in the lift coefficient curve slope as the Mach number was increased. This was related to changes in the deflection of the airfoil resulting from the response of the structure to aerodynamic forces.

The proposed framework extends capabilities to handle unsteady flow conditions. The inclusion of airfoil morphing, and aeroelasticity effect resulted in significant changes in the C_l and C_m hysteresis. For pitching airfoils, aeroelastic effects lead a slight smaller Cl_{max} compared to the rigid airfoil by an amount of $\Delta C_l = 0.05$. The fluid-structure interaction became more pronounced, when the airfoil is actively morphed. The decrease of the Cl_{max} was magnified to $\Delta C_l = 0.18$. The changes were observed not only for the lift coefficient but also for the pitching moment, for pitching airfoil the C_m hysteresis exhibited a change in slope that resulted in positive C_m values. This indicated the induction of a nose-up moment by aeroelastic effects. Incorporating the active camber morphing, the slope of the C_m hysteresis changes drastically. Although C_m values remained negative, the width of the hysteresis greatly magnified and results higher magnitude of pitching moments. The coupled case exhibited smaller pitching moments in terms of magnitude compared to the CFD standalone simulations.

In summary, the investigations showed that a significant fluid-structure interaction occurred in the active camber deformation approach, specifically for the structure demonstrated. The standalone CFD simulations were insufficient to represent the aerodynamic characteristics of actively morphing airfoils and aeroelastic effects must be considered.

Author contact:
Muhammed Kürşat Yurt kursat.yurt@tum.de
Amine Abdelmoula amine.abdelmoula@tum.de
Jonas John jonas.john@tum.de
İlkay Yavrucuk ilkay.yavrucuk@tum.de

ACKNOWLEDGMENT

This work is supported by the German Federal Ministry for Economic Affairs and Climate Action through the German Aviation Research Program LuFo VI-2 in the project ARCTIS under grant number 20E2108A.

Federal Ministry for Economic Affairs and Climate Action

5 REFERENCES

[1]Roth, D., Enenkl, B., and Dieterich, O., "Active rotor control by flaps for vibration reduction-full scale demonstrator and first flight test results," 2006.

[2]Hunsaker, D. F., Reid, J., and Moorthamers, B., "Geometry and Aerodynamic Performance of Parabolic Trailing-Edge Flaps," 2018.

[3]Woods, B. K. S., Bilgen, O., and Friswell, M. I., "Wind tunnel testing of the fish bone active camber morphing concept," *Journal of Intelligent Material Systems and Structures*, 2014.

[4]Woods, B. K. S. and Friswell, M. I., "Preliminary Investigation of a Fishbone Active Camber Concept," *ASME 2012 Conference on Smart Materials, Adaptive Structures and Intelligent Systems*, 2012.

[5]Woods, B. K. S. and Friswell, M. I., "Fluid-Structure Interaction Analysis of the Fish Bone Active Camber Mechanism," 2013.

[6]Woods, B. K. S., Fincham, J. H. S., and Friswell, M. I., "Aerodynamic Modelling of the Fish Bone Active Camber Morphing Concept," *RAeS Applied Aerodynamics Conference*, 2014.

[7]Woods, B. K. S. and Friswell, M. I., "Structural Characterization of the Fish Bone Active Camber Morphing Airfoil," 2014.

[8]Woods, B. K. S., Dayyani, I., and Friswell, M. I., "Fluid/Structure-Interaction Analysis of the Fish-Bone-Active-Camber Morphing Concept," *Journal of Aircraft*, Vol. 52, No. 1, Jan. 2015, pp. 307–319.

[9]Rauleder, J., van der Wall, B. G., Abdelmoula, A., Komp, D., Kumar, S., Ondra, V., Titurus, B., and Woods, B. K. S., "Aerodynamic Performance of Morphing Blades and Rotor Systems," *AHS International 74th Annual Forum & Technology Display*, , No. May, 2018.

[10]Komp, D., Kumar, S., Abdelmoula, A., Hajek, M., and Rauleder, J., "Investigation of active rotor design and control for performance improvement," *Vertical Flight Society 75th Annual Forum*, 2019.

[11]Komp, D., Kumar, S., Hajek, M., and Rauleder, J., "Effect of active camber morphing on rotor performance and control loads," *Aerospace Science and Technology*, Vol. 108, 2021, pp. 106311.

[12]Komp, D., Hajek, M., and Rauleder, J., “Rotor Performance Enhancements with Spanwise Varying Active Camber Morphing,” *AIAA Scitech 2021 Forum*, 2021, p. 0200.

[13]Kumar, S., Komp, D., Hajek, M., and Rauleder, J., “Effect of Active Camber on Rotor Noise, Power and Hub Vibration,” *AIAA Scitech 2021 Forum*, 2021, p. 1927.

[14]Abdelmoula, A., Platzer, S., Hajek, M., and Rauleder, J., “Numerical investigation of the effects of dynamic camber variation on the airfoil characteristics of a pitching rotor airfoil,” *AIAA Scitech 2020 Forum*, 2020, p. 1302.

[15]Newmark, N. M., “A Method of Computation for Structural Dynamics,” *Journal of the Engineering Mechanics Division*, Vol. 85, No. 3, July 1959, pp. 67–94.

[16]Economon, T. D., Palacios, F., Copeland, S. R., Lukaczyk, T. W., and Alonso, J. J., “SU2: An Open-Source Suite for Multiphysics Simulation and Design,” *AIAA Journal*, Vol. 54, No. 3, March 2016, pp. 828–846.

[17]Bungartz, H.-J., Lindner, F., Gatzhammer, B., Mehl, M., Scheufele, K., Shukaev, A., and Uekermann, B., “preCICE–a fully parallel library for multi-physics surface coupling,” *Computers & Fluids*, Vol. 141, 2016, pp. 250–258.

[18]Dwight, R. P., “Robust Mesh Deformation using the Linear Elasticity Equations,” *Computational Fluid Dynamics 2006*, Springer Berlin Heidelberg, 2009, pp. 401–406.

[19]Komp, D., Kumar, S., Hajek, M., and Rauleder, J., “Effect of active camber morphing on rotor performance and control loads,” *Aerospace Science and Technology*, Vol. 108, Jan. 2021, pp. 106311.

[20]Drela, M., “XFOIL: An analysis and design system for low Reynolds number airfoils,” *Low Reynolds Number Aerodynamics: Proceedings of the Conference Notre Dame, Indiana, USA, 5–7 June 1989*, Springer, 1989, pp. 1–12.

[21]Jain, R., Yeo, H., and Chopra, I., “Examination of Rotor Loads due to On-Blade Active Controls for Performance Enhancement,” *Journal of Aircraft*, Vol. 47, No. 6, Nov. 2010, pp. 2049–2066.